Journal of Advances in Modeling Earth Systems

Supporting Information S1 for

A novel back-calculation approach to estimate ocean anthropogenic carbon using carbon-based data and a Total Matrix Intercomparison method

M. López-Mozos[1,2]*, F.F. Pérez[1], L.I. Carracedo[3], G. Gebbie[4], A. Velo[1]

[1] Instituto de Investigaciones Marinas (IIM-CSIC), 36208, Vigo, Spain

[2] Facultad de Ciencias del Mar, Universidade de Vigo, Spain.

[3] Univ Brest, CNRS, Ifremer, IRD, Laboratoire d'Océanographie Physique et Spatiale (LOPS), IUEM, F29280, Plouzané, France.

[4] Department of Physical Oceanography, Woods Hole Oceanographic Institution, Woods Hole, Massachusetts 02543

Corresponding author: Marta López-Mozos (mlopezm@iim.csic.es)

Contents of this file

Supporting Information Text 1: Steady-state anthropogenic carbon

According to the established REgional Carbon Cycle Assessment and Processes (RECCAP2) Ocean Component division, and following DeVries et al. (2023), the globally integrated sea-air CO_2 flux ($F_{sea\text{-}air}$) is a combination of natural and anthropogenic components:

$$F_{sea\text{-}air} = F_{nat} + F_{ant} \quad \text{(Eq 1)}$$

hence in the ocean interior, $$DIC = DIC_{nat} + C_{ant} \quad \text{(Eq 2)}$$

and evaluating ocean interior changes $$\Delta DIC = \Delta DIC_{nat} + \Delta C_{ant} \quad \text{(Eq 3)}$$

Anthropogenic sea-air CO_2 flux (F_{ant}) and anthropogenic DIC (C_{ant}) result from rising atmospheric CO_2 since the pre-industrial era because of human-actions. If we consider that the release of this excess CO_2 does not interfere with climate and, therefore, ocean circulation is not altered as a result (e.g., no ocean warming), then this excess, or C_{ant}, would increase in the ocean proportionally to its increase in the atmosphere (Gammon et al., 1982). Gruber et al. (2019) actually found that C_{ant} inventory (total C_{ant} amount) changes between 1994 and 2007 were spatially correlated with C_{ant} inventory in 1994, concluding that this relationship is consistent with the quasi-exponential and multidecadal nature of the anthropogenic perturbation of the global carbon cycle, and establishing that C_{ant} is in a *transient steady state* (Gammon et al., 1982). The concept of *transient steady state* (Gammon et al., 1982) establishes that for a conservative - and transient - tracer that increases exponentially in the atmosphere and enters the ocean surface, mixing vertically downward by both diffusive and advective processes, its concentration at each depth also increases exponentially in time. Its vertical distribution normalised to its mixed layer concentration, becomes, nevertheless, steady, and can be described by a constant diffuse-advective scale depth.

However, anthropogenic CO_2 release into the atmosphere feedbacks climate, as global warming is partly due to CO_2 atmospheric excess, as it behaves as a greenhouse gas. Therefore, despite being little (DeVries et al., 2023), there is a fraction in F_{ant} resulting from climate change (as major changes on ocean stratification due to ocean warming) that constitute the non-steady component. Then:

$$F_{ant} = F_{ant}^{ss} + F_{ant}^{ns} \quad \text{(Eq 4)}$$

often noted as $F_{ant} = F_{ant,CO2} + F_{ant,climate}$, according to DeVries et al. (2023) nomenclature,

hence in the ocean interior, $$C_{ant} = C_{ant}^{ss} + C_{ant}^{ns} \quad \text{(Eq 5)}$$

Similarly, the natural sea-air CO_2 flux (F_{nat}) fraction includes a preindustrial component at steady-state (F_{nat}^{ss}) that does not change over time (DeVries et al. 2023), and a non steady state component (F_{nat}^{ns}) that results from how natural DIC is changing due to climate

change effect (again, we can use ocean warming as example) or because natural non steady-state sink-sources. Therefore:

$$F_{nat} = F_{nat}^{ss} + F_{nat}^{ns} \quad \text{(Eq 6)}$$

hence in the ocean interior, $DIC_{nat} = DIC_{nat}^{ss} + DIC_{nat}^{ns}$ (Eq 7)

In the North Atlantic, Tanhua et al. (2006) found that C_{ant} is in *transient steady state*, meaning that the C_{ant} concentration increases proportionally over time through the whole water column in a manner that is directly related to the time-dependent surface concentration. Transient tracers are chemicals introduced by human activity, hence they are anthropogenic tracers, that gradually invade the ocean from surface to depth, either being conservative or non-conservative. Chlorofluorocarbons (CFCs) are conservative transient tracers that are extremely helpful for estimating ocean ventilation and derive a statistical description of the *age distribution* (Hall et al., 2002). Indeed, Waugh et al. (2006) proposed a global ocean C_{ant} reconstruction by considering C_{ant} as a conservative tracer that could be reconstructed from ocean circulation transport, relying on a transit time distribution (TTD) based on CFCs. Later, Khatiwala et al. (2009) refined this approach by improving the Green's Function behind it, proving also a global steady-state C_{ant} reconstruction, since the mixing of waters of different ages and end-member water types was accounted for by using multiple transient and steady tracers to constraint the age distributions, neglecting possible ocean circulation variability. The *steady-state* ocean circulation provided by the data-assimilation OCIM model, that is an abiotic ocean carbon cycle model, allowed DeVries (2014; 2022) to reconstruct C_{ant} in *steady-state* globally, by considering it as a conservative tracer and improving the mixing scheme resolution compared to Khatiwala et al. (2009) reconstruction. All these C_{ant} reconstructions are hence based on a steady-state mixing framework; therefore, and because of the constant circulation assumption, they do not include circulation-driven C_{ant} variability (i.e., the non steady-state component), that, e.g., Global Ocean Biogeochemical Models (GOBMs) do (DeVries et al., 2023). In conclusion, all these transient tracer-based methodologies provide C_{ant} reconstructions that only capture the *steady-state* component of the C_{ant} pool.

In this work, we present a back-calculation approach to estimate C_{ant}, resulting in a global and climatological C_{ant} reconstruction in steady-state, centred in 1995. First, the back-calculation approach followed is relatively insensitive to changes in the natural carbon cycle (Matsumoto and Gruber, 2005), even if they are driven by anthropogenic climate change. An explicit example from Matsumoto and Gruber (2005) is that *a slowdown in circulation that causes waters to spend more time away from the surface would result in an anomalous accumulation of DIC from respiration which will be reflected in a larger change in the biogeochemical correction.* Secondly, we use climatological MCS data, specifically we part from climatological DIC centred in 1995 (Broullón et al. 2020) - hence we do not evaluate any change of DIC over time except the change from preindustrial to 1995 - and subtract processes until getting the anthropogenic fraction in the DIC pool. In more detail, we estimate such processes from climatological data of several properties, centred in 1995, meaning that we neither assess any property change over time, then not assess C_{ant} changes but absolute C_{ant} values. Lastly, we use the transport operators of a

steady-state model (TMI) to estimate the preformed conditions of non-conservative variables, and/or for reconstructing interior ocean properties from their surface distribution. This means that any preformed variable or reconstruction in our study is also in steady-state. Therefore, and as in previous works, as Sabine et al. (2004), Waugh et al. (2006), Khatiwala et al. (2009), or DeVries (2014; 2022), our C_{ant} reconstruction only captures the steady-state component of the C_{ant} pool that, despite not being the total C_{ant} fraction, has been shown to be much larger (~98%) than the non steady-state C_{ant} (~2%; DeVries et al., 2023).

Supporting Information references

DeVries, T. (2014). The oceanic anthropogenic CO2 sink: Storage, air-sea fluxes, and transports over the industrial era. *Global Biogeochemical Cycles*, *28*(7), 631-647. https://doi.org/10.1002/2013GB004739

Gammon, R. H., Cline, J., & Wisegarver, D. (1982). Chlorofluoromethanes in the northeast Pacific Ocean: Measured vertical distributions and application as transient tracers of upper ocean mixing. *Journal of Geophysical Research: Oceans*, *87*(C12), 9441-9454. https://doi.org/10.1029/JC087iC12p09441

Tanhua, T., Biastoch, A., Körtzinger, A., Lüger, H., Böning, C., & Wallace, D. W. (2006). Changes of anthropogenic CO_2 and CFCs in the North Atlantic between 1981 and 2004. *Global biogeochemical cycles*, *20*(4). https://doi.org/10.1029/2006GB002695

Equation S1.

$$C_{ant} = C_T - \frac{1}{r_{o:c}} \cdot (AOU - AOU^{\circ}) + denitrif. - \frac{1}{2} \cdot \left[A_T - A_T^{\circ} + (AOU - AOU^{\circ}) \cdot \left(\frac{1}{r_{o:n}} + \frac{1}{r_{o:p}}\right)\right] - C_T^{\pi SAT} \ldots - \Delta C_{dis}^{\pi}$$

$$C_{ant-GSS96} = C_T - \frac{1}{r_{o:c}} \cdot (AOU) + denitrif - \frac{1}{2} \cdot \left[A_T - A_T^{\circ} + (AOU) \cdot \left(\frac{1}{r_{o:n}} + \frac{1}{r_{o:p}}\right)\right] - C_T^{\pi SAT} - \Delta C_{dis}^{\pi GSS96}$$

(1) $C_{ant} = C_{ant-GSS96}$

$$\cancel{C_T} - \frac{1}{r_{o:c}} \cdot (\cancel{AOU} - AOU^{\circ}) \cancel{+ denitrif.} - \frac{1}{2} \cdot \left[\cancel{A_T - A_T^{\circ}} + (\cancel{AOU} - AOU^{\circ}) \cdot \left(\frac{1}{r_{o:n}} + \frac{1}{r_{o:p}}\right)\right] \cancel{- C_T^{\pi SAT}} - \Delta C_{dis}^{\pi} =$$

$$\cancel{C_T} - \cancel{\frac{1}{r_{o:c}} \cdot (AOU) + denitrif} - \frac{1}{2} \cdot \left[\cancel{A_T - A_T^{\circ}} + (AOU) \cdot \left(\cancel{\frac{1}{r_{o:n}} + \frac{1}{r_{o:p}}}\right)\right] \cancel{- C_T^{\pi SAT}} - \Delta C_{dis}^{\pi GSS96}$$

(2) $-\frac{1}{r_{o:c}} \cdot (-AOU^{\circ}) - \frac{1}{2} \cdot \left[(-AOU^{\circ}) \cdot \left(\frac{1}{r_{o:n}} + \frac{1}{r_{o:p}}\right)\right] - \Delta C_{dis}^{\pi} = -\Delta C_{dis}^{\pi GSS96}$

(3) $$\Delta C_{dis}^{\pi} = AOU^{\circ} \cdot \left(\frac{1}{r_{o:c}} + \frac{1}{2 \cdot r_{o:n}} + \frac{1}{r_{o:p}}\right) + \Delta C_{dis}^{\pi GSS96}$$

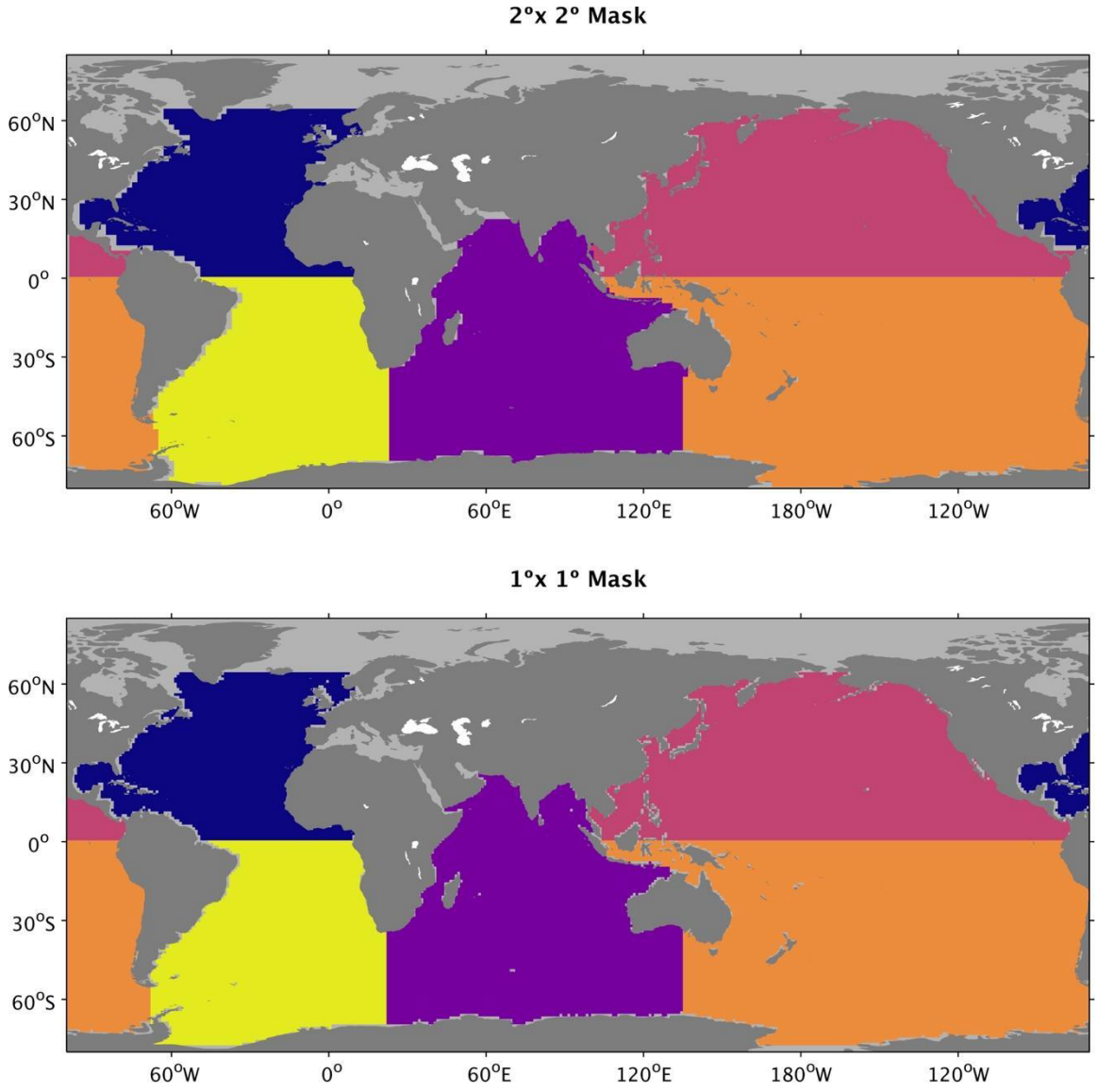

Figure Supplementary 1. Masks created in 1ºx1º and 2ºx2º grids to compute total C_{ant} inventories. The five regions are: North Atlantic (dark blue), South Atlantic (yellow), North Pacific (pink), South Pacific (orange) and Indian Ocean (purple). For the North Atlantic and North Pacific regions, northernmost latitude was set at 65ºN. The Southern Ocean longitude limits between the Atlantic to Indian, Indian to Pacific and Pacific to Atlantic are 22.5ºE, 134.5ºE and 69.5ºW respectively. The 1ºx1º mask was interpolated to a 2ºx2º grid through DIVA. The 1ºx1º was applied to Sabine et al., (2004), Lauvset et al., (2016), DeVries (2022) and Khatiwala et al., (2009) product. The 2ºx2º mask was used for TrOCA method and the results presented in this issue. The information of the region areas is presented in Supplementary Table 1.

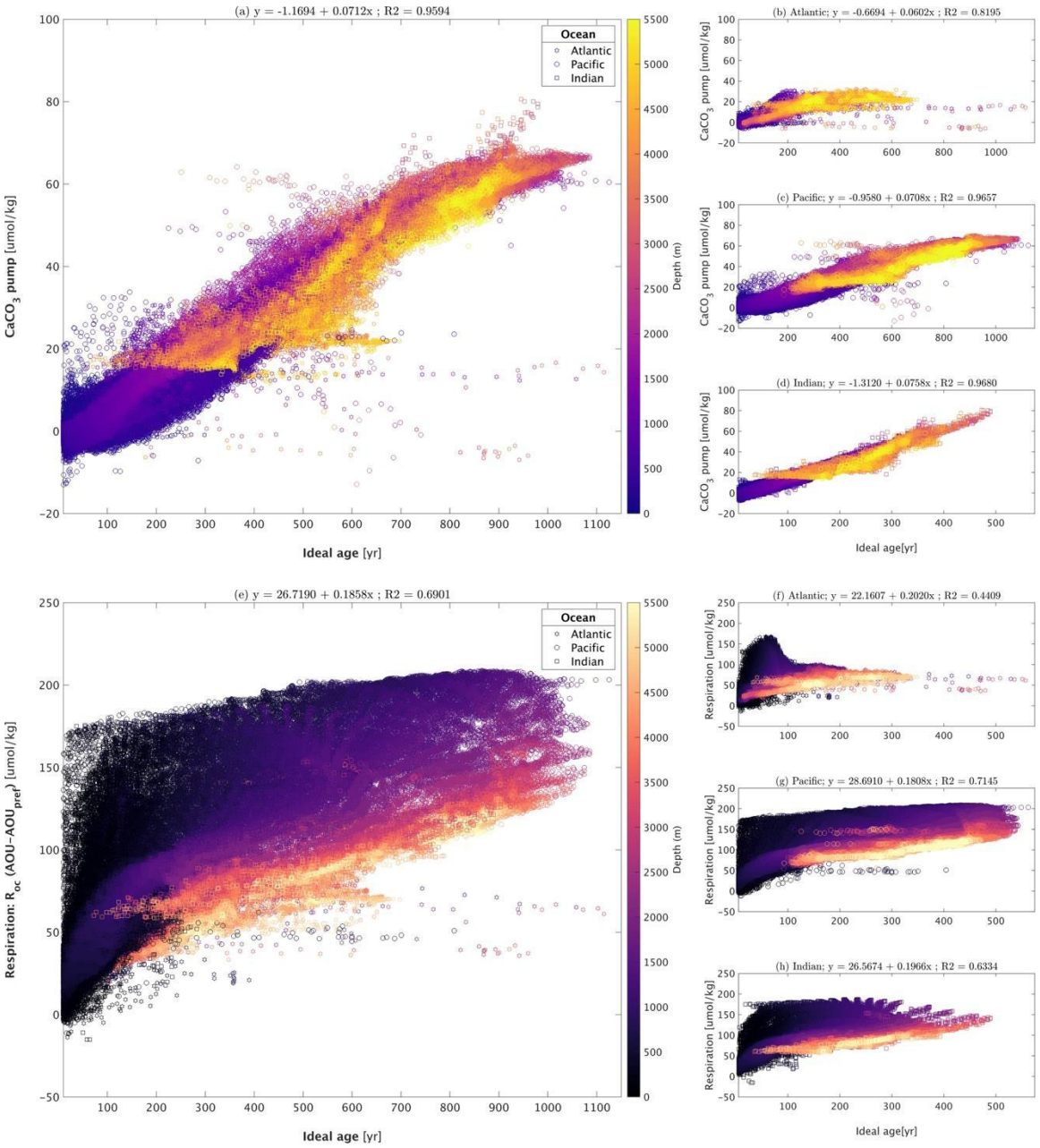

Figure Supplementary 2. (a) (Top left) Scatter plot of ideal age - from the TMI - versus carbonate pump, expressed in carbon concentrations. Point's colour represents different depths, and point shapes three ocean basins (hexagram-Atlantic, circle-Pacific, square-Indian). (Top right) Same as top left but for each ocean individually: **(b)** Atlantic **(c)** Pacific **(d)** Indian. **(e)** (Bottom left) Scatter plot of ideal age - from the TMI - versus respiration. Point's colour represents different depths and point shapes three ocean basins (hexagram-Atlantic, circle-Pacific, square-Indian). (Bottom right) Same as bottom left, but for each ocean individually: **(f)** Atlantic **(g)** Pacific **(h)** Indian.

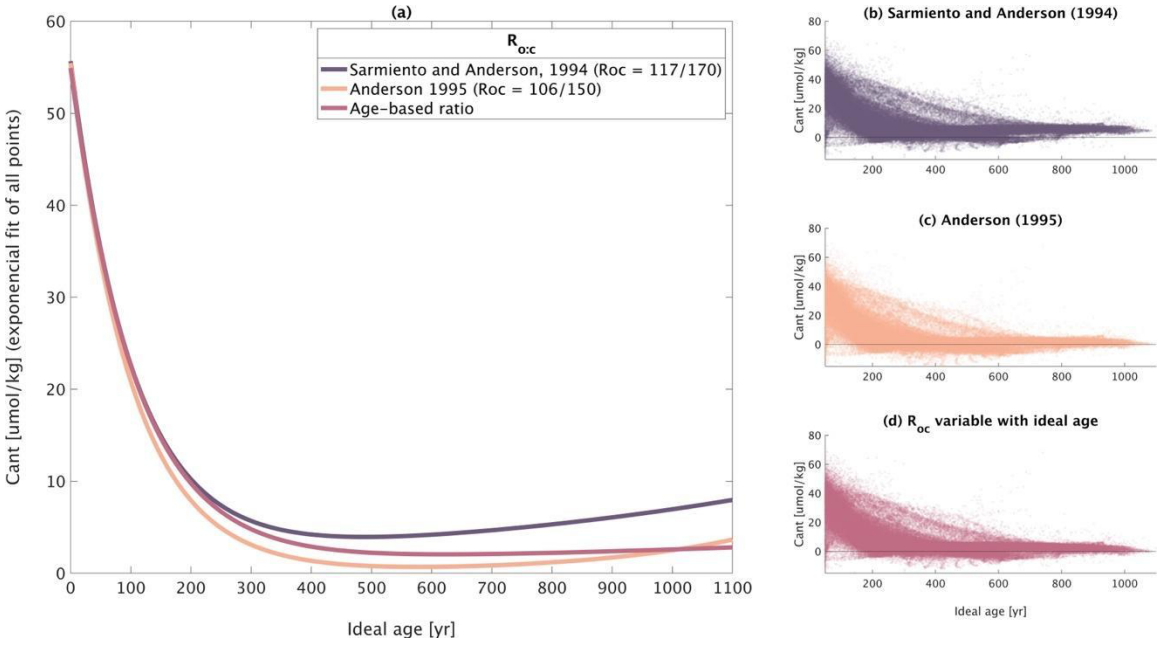

Figure Supplementary 3. Anthropogenic carbon trend evolution versus ideal age from the TMI, using three different oxygen to carbon stoichiometric ratios. **Left) (a)** Exponential fit of C_{ant} values (from surface to bottom = 5500m; -20 < C_{ant} < 70 and 50 < ideal age < 1100). **Right) (b, c ,d)** Individual C_{ant} data scatter plots according to the stoichiometric ratio used (-20 < C_{ant} < 70 and 50 < ideal age < 1100).

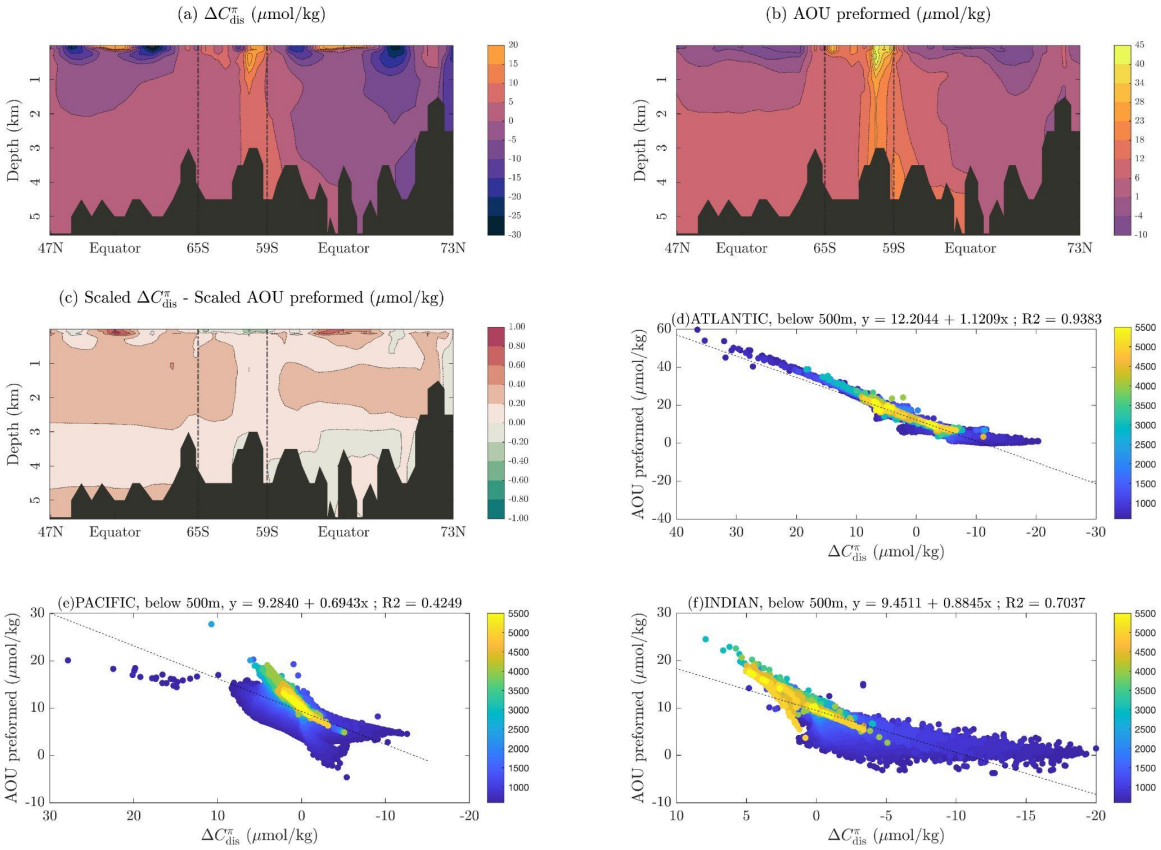

Figure Supplementary 4. Panel (a) and (b). Transoceanic section from 73ºN Atlantic up to 47ºN Pacific, connecting the start-end section through the Southern Ocean (SO). The two vertical lines define the end of the Atlantic basin through the SO (SO-Atl 59ºS), and the beginning of the Pacific basin (SO-Pac 65ºS). Panel **(a)** shows vertical distribution of sea-air preindustrial CO_2 disequilibrium, deep-reconstructed with the TMI, derived from Khatiwala et al., (2009) surface boundary condition. Panel **(b)** shows sea-air oxygen disequilibrium, computed at surface from saturation and observations, centered in 1995, and propagated into ocean interior through the TMI. Most often, in high latitudes, the CO_2 and O_2 sea-air equilibration is not fully complete when the water masses sink into the deep ocean because of the slow equilibration (Gruber et al. 1996; Ito et al., 2004). This incomplete equilibration results in negative values of CO_2 and O_2 sea-air disequilibrium (undersaturation) that spread around the deep Atlantic, since the recently formed NADW is the dominating water mass in the deep layers (Liu and Tanhua, 2021). The regions of central water mass formation in both the Atlantic and Pacific basins exhibit the most intense negative imbalances. Conversely, equatorial upwelling zones and the Antarctic divergence region experience oversaturated water masses, likely due to incomplete carbon outgassing as they reach the surface. **Panel (c)** Difference between sea-air pre-industrial CO_2 disequilibrium and sea-air oxygen disequilibrium, both previously 0-1 scaled. **Panel (d).** Linear regression of sea-air preindustrial CO_2 disequilibrium versus sea-air oxygen disequilibrium in the Atlantic Ocean, with data from depths > 500m. Colour points represent depth, and the black dashed line the adjusted regression line. **Panel (e).** Same as D but for the Pacific Ocean. **Panel (f).** Same as D but for the Indian Ocean.

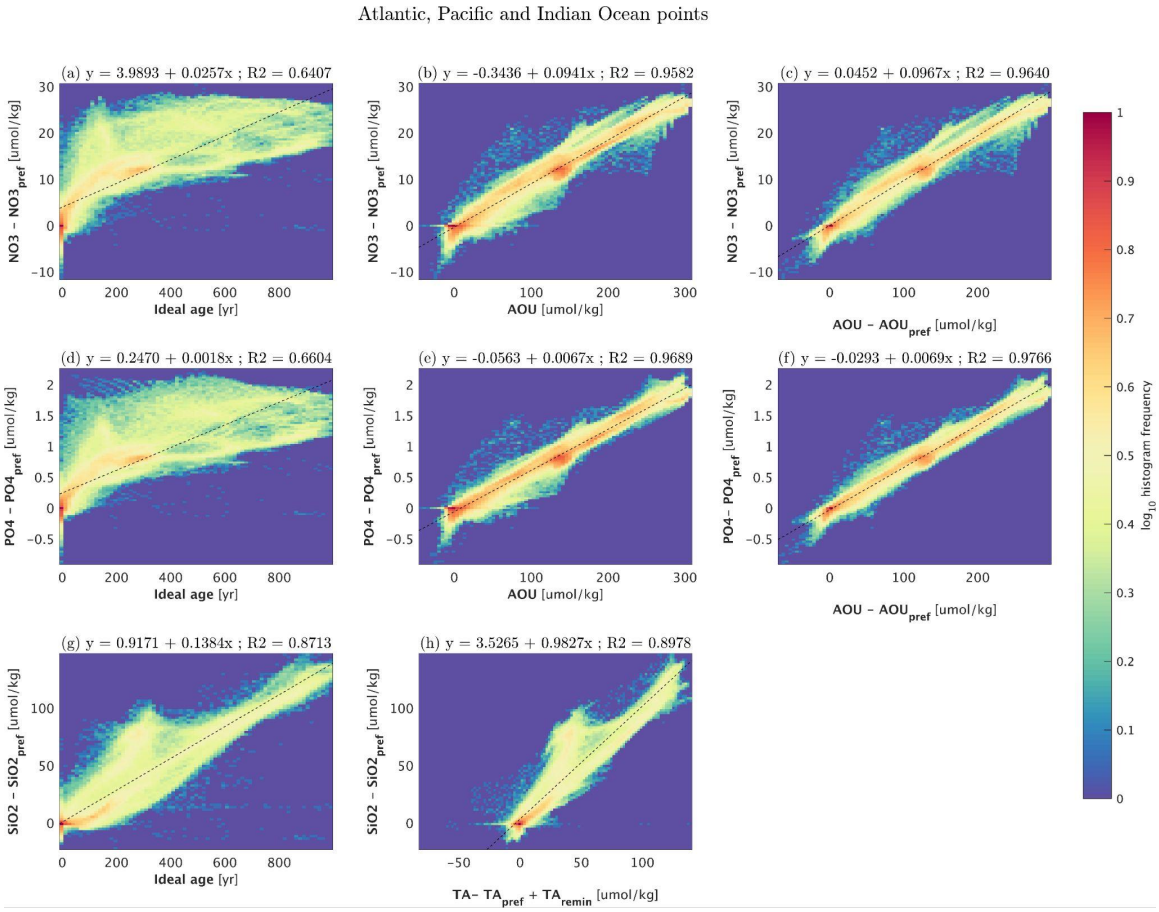

Figure Supplementary 5. X-Y histogram plots, with their respective linear regression adjustment of **(a)** Ideal TMI age versus $NO_3 - NO_3^o$, **(b)** AOU versus $NO_3 - NO_3^o$, **(c)** AOU – AOU^o versus $NO_3 - NO_3^o$, **(d)** Ideal TMI age versus $PO_4 - PO_4^o$, **(e)** AOU versus $PO_4 - PO_4^o$, **(f)** AOU – AOU^o versus $PO_4 - PO_4^o$, **(g)** Ideal TMI age versus $SiO_2 - SiO_2^o$, and **(h)** carbonate pump versus $SiO_2 - SiO_2^o$.

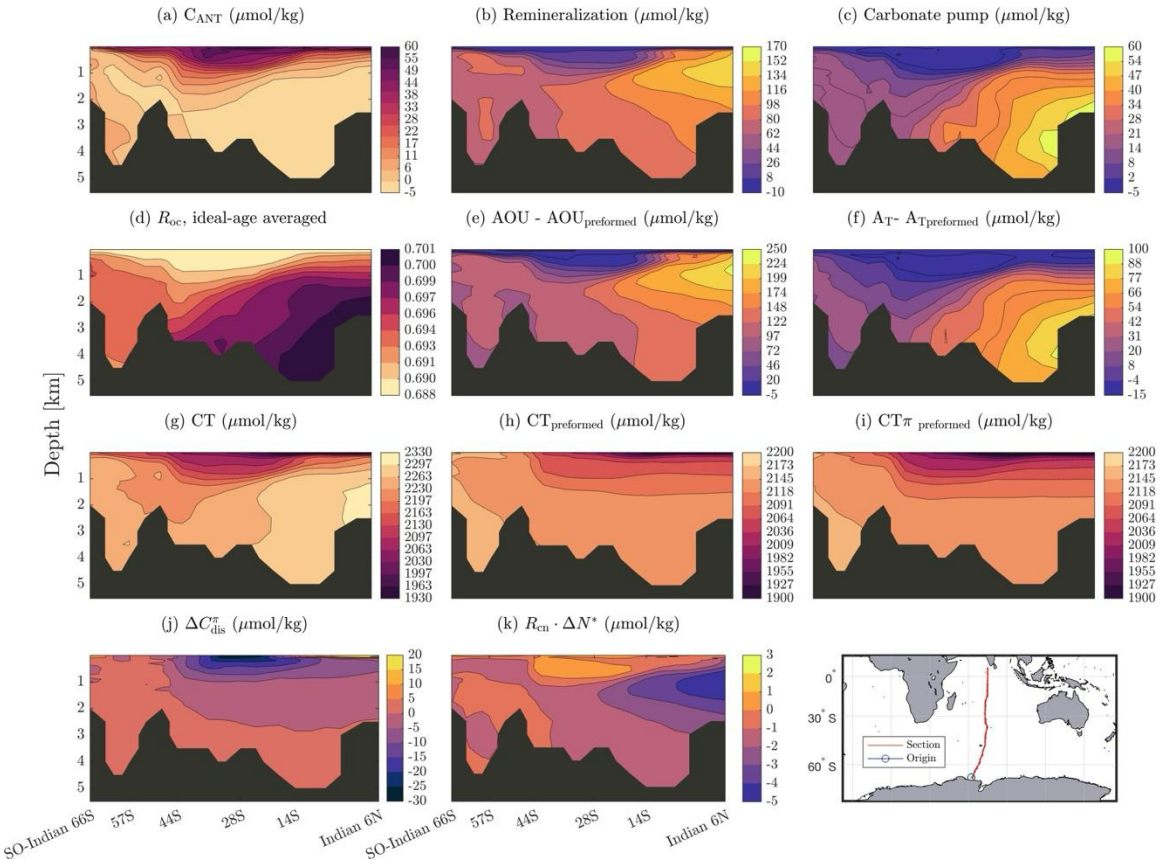

Figure Supplementary 6. Indian Ocean section, showing vertical C_{ant} distribution and biogeochemical and physicochemical processes, from 66ºS to 6ºN. Panels: (**a**) Anthropogenic carbon (C_{ant}), (**b**) remineralization term (see *Section 2.1*), (**c**) carbonate pump term (*see Section 2.1*), converted to carbon concentrations, (**d**) age-based oxygen to carbon stoichiometric ratio, (**e**) difference between AOU and preformed AOU, (**f**) difference between Total Alkalinity and preformed Total Alkalinity, (**g**) total inorganic carbon from Broullón et al., (2020), (**h**) preformed total inorganic carbon, from subtracting biological panels B and C to panel G, (**i**) pre-industrial preformed total inorganic carbon, (j) sea-air CO_2 disequilibrium and, (**k**) denitrification process, expressed in carbon concentrations.

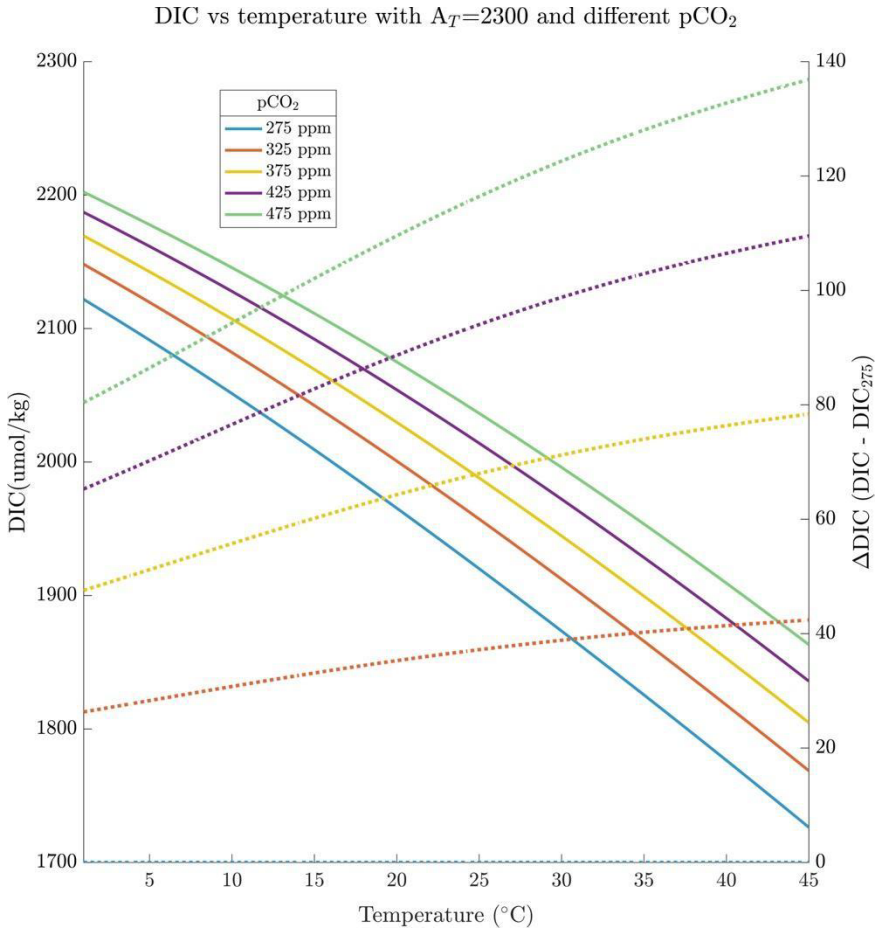

Figure Supplementary 7. Relationship between temperature variation (X-axis) and C_T content (or DIC, Y-axis left) and C_T content – C_T at 275 ppm (i.e., $C_{ant;}$ dashed lines; Y-axis right). These relationships are shown for 5 scenarios with different pCO_2 (colour lines; 275, 325, 375, 425 and 475 ppm), keeping a constant alkalinity in all (A_T = 2300 µmol kg^{-1}). The C_T concentration decreases as temperature increases. Even so, when observing the difference between the colour curves, the higher the temperature, the greater the difference, which explains why warmer water masses capture more C_{ant}.

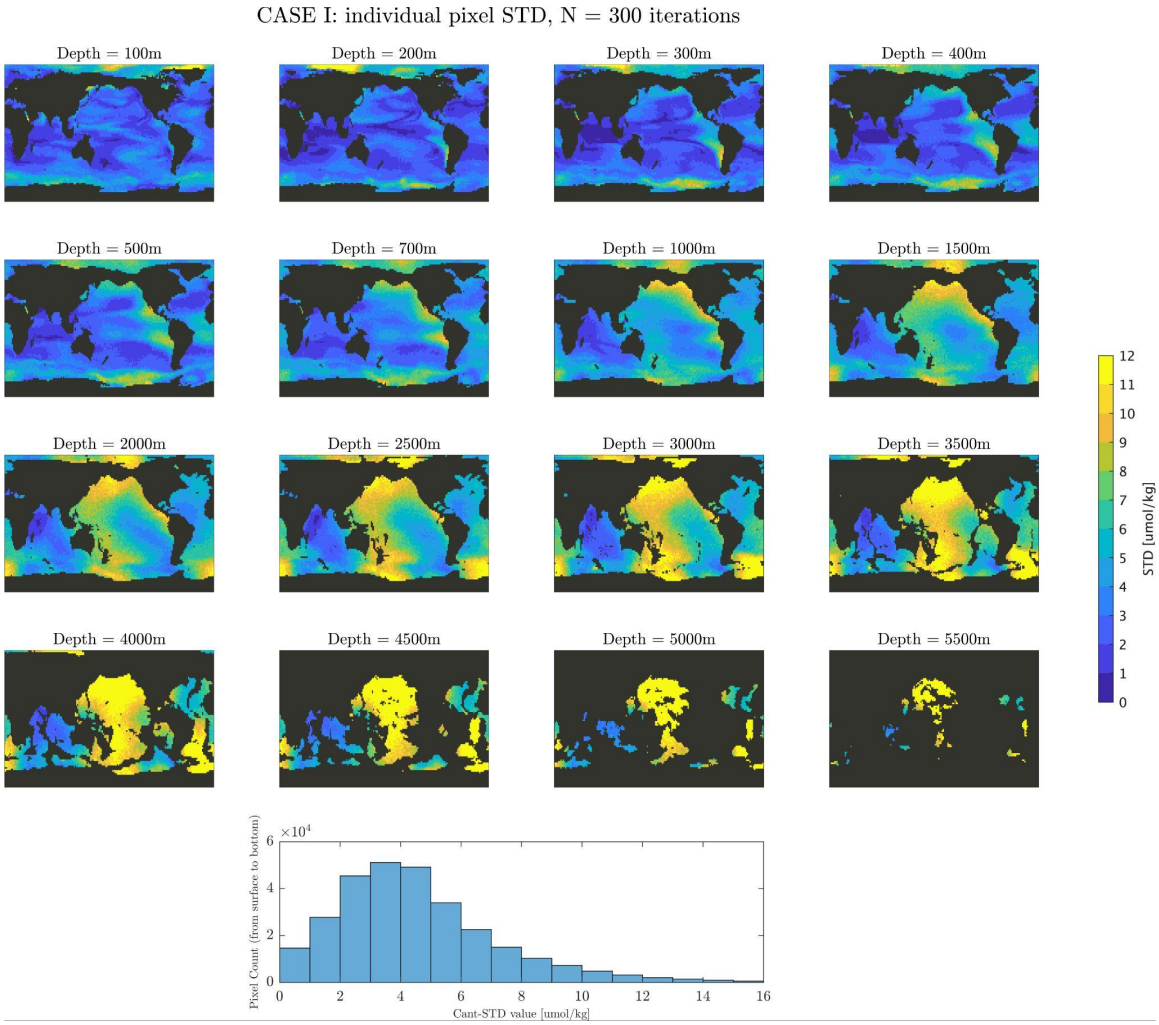

Figure Supplementary 8. C_{ant} standard deviations (STD) by selected depth horizons (in µmol kg^{-1}), computed as the STD at each grid point of the 300 simulations of the sensitivity analysis *Case I* . **Bottom)** Histogram of C_{ant} STD values (µmol kg^{-1}), from 300 simulations of the *Case I*, in all vertical levels (surface to 5500m).

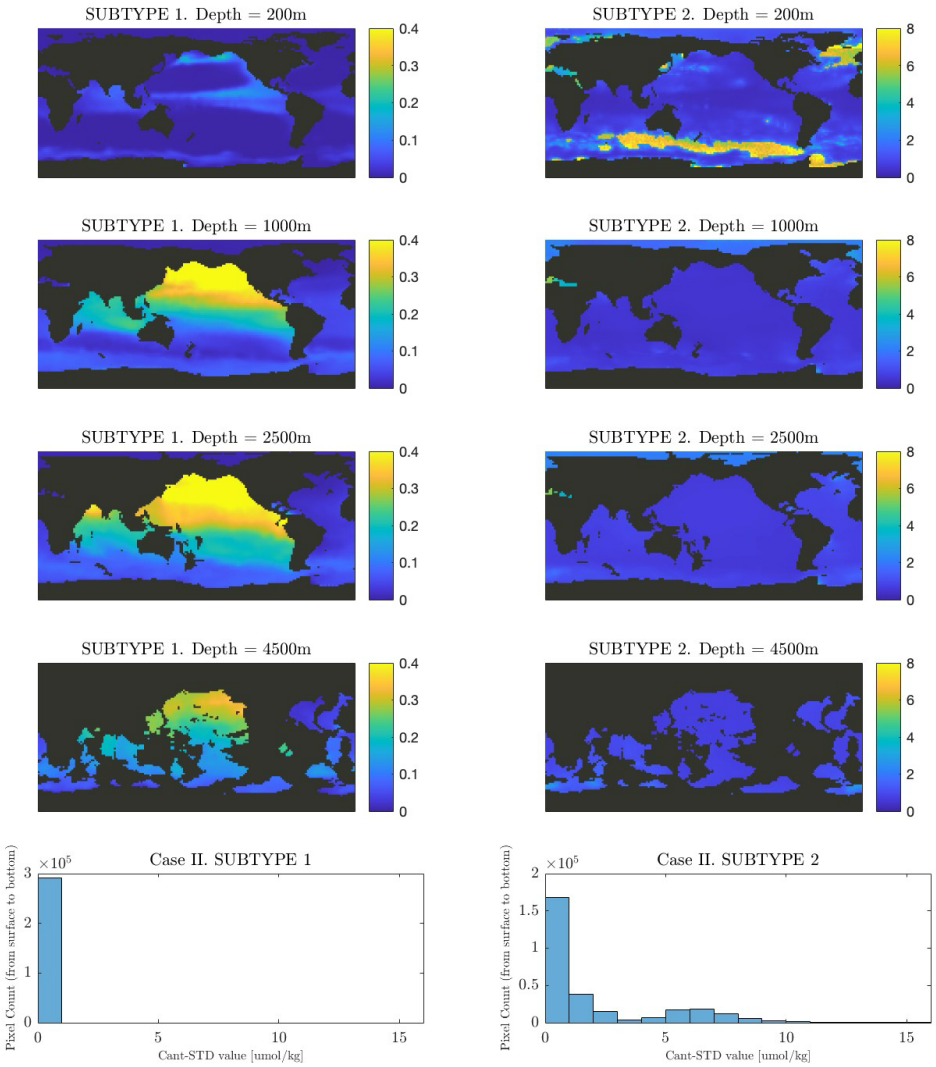

Figure Supplementary 9. C_{ant} standard deviations (STD) by selected depth horizons (in µmol kg^{-1}), computed as the STD at each grid point of the 300 simulations of the sensitivity analysis *Case II*. There are two columns showing, from left to right, *Case II - subtype 1* and *Case II - subtype* 2. **Bottom)** Histogram of C_{ant} STD values (µmol kg^{-1}), from 300 simulations of each subtype, in all vertical levels (surface to 5500m).

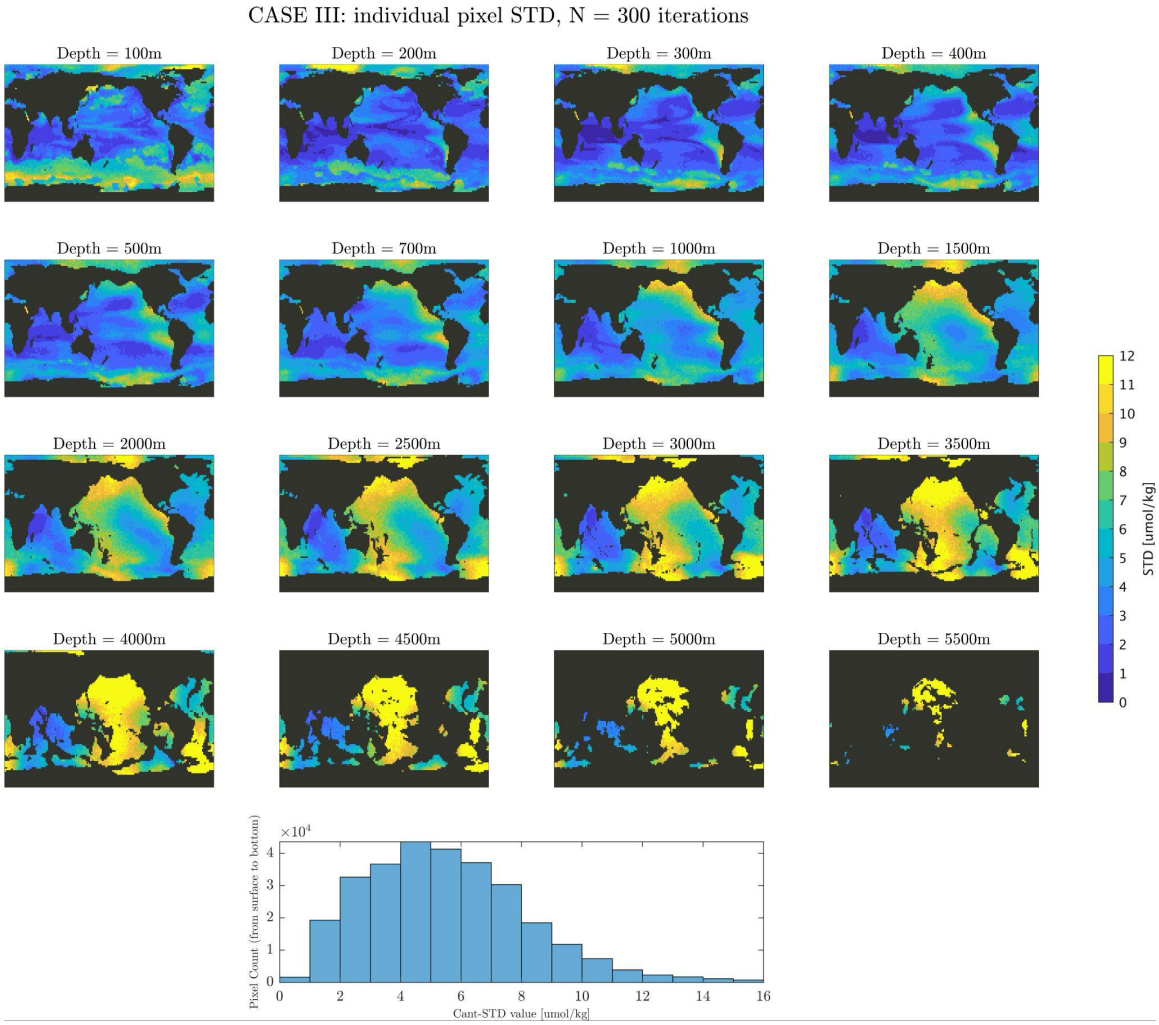

Figure Supplementary 10. C_{ant} standard deviations (STD) by selected depth horizons (in µmol kg^{-1}), computed as the STD at each grid point of the 300 simulations of the sensitivity analysis *Case III*. **Bottom)** Histogram of C_{ant} STD values (µmol kg^{-1}), from 300 simulations of the *Case III*, in all vertical levels (surface to 5500m).

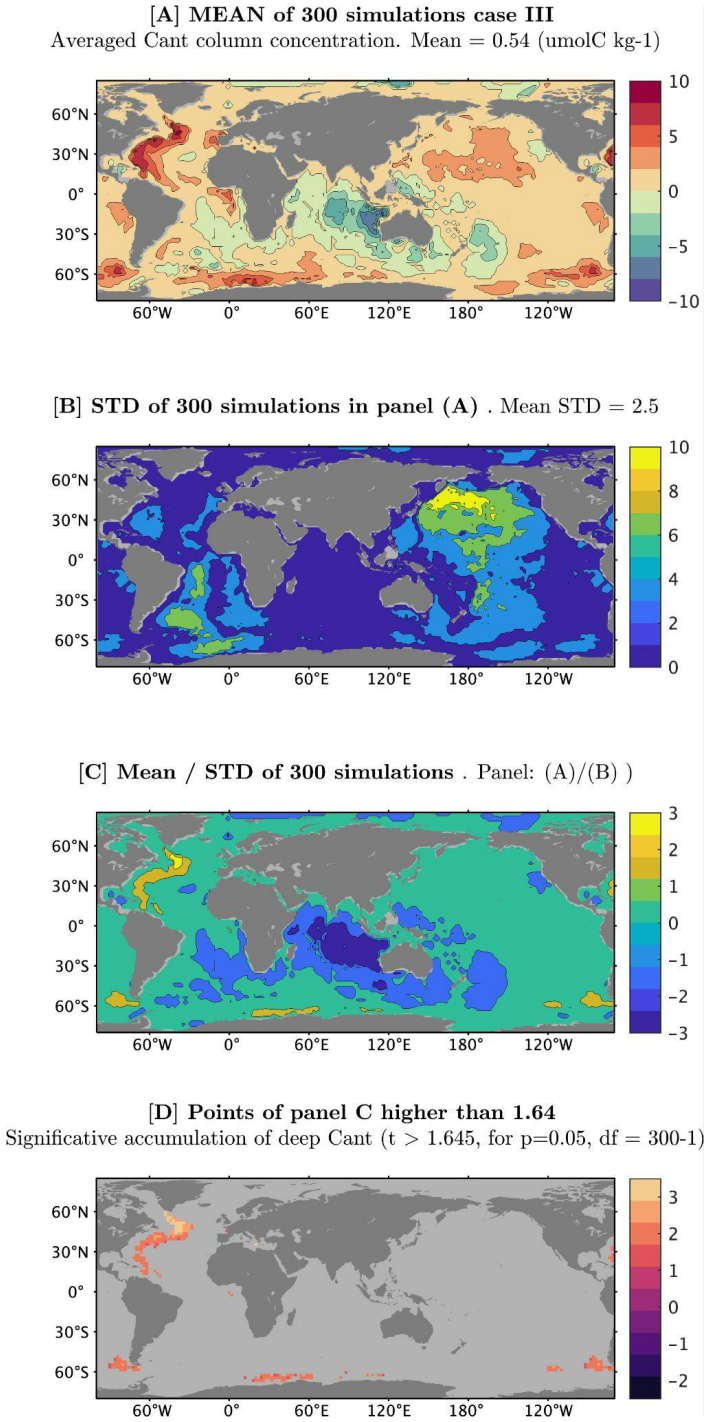

Figure Supplementary S11. **Panel (a)** Averaged C_{ant} column concentration integrated below 3500m (µmolC kg^{-1}) – mean of 300 simulations of *Case III*. **Panel (b)** Averaged C_{ant} column concentration integrated below 3500m (µmolC kg^{-1}) – STD of 300 simulations of *Case III*. **Panel (c)** Panel (a) over panel (b). **Panel (d)** Deep-ocean regions where our method can attribute that presence of C_{ant} is distinguishable from zero. This is, with degrees of freedom (*df*) = 300 - 1 and a *p-value* > 0.05, the *t-student* is cut off at 1.645 as the values that are significantly different from 0. Thus, panel (d) shows the values of panel C that are above this threshold.